International Journal of Nanoelectronics and Materials
IJNeaM
ISSN 1985-5761 | E-ISSN 2232-1535

Mutual coupling reduction between FSS decoupling structure and nanoantenna array-elements in THz multi-band plasmonic UM-MIMO

Ammar Mohammad Issa Banat[a], Khairul Najmy Abdul Rani[b,c], Tijjani Adam[a,b,d*], Alaa Kamal Yousif Dafhalla[e]

[a]*Institute of Nano Electronic Engineering, Universiti Malaysia Perlis, 01000 Kangar, Perlis, Malaysia*
[b]*Faculty of Electronic Engineering & Technology, Universiti Malaysia Perlis, Pauh Putra Campus, 02600 Arau, Perlis, Malaysia*
[c]*Advanced Communication Engineering (Centre of Excellence), Universiti Malaysia Perlis, 01000 Kangar, Perlis, Malaysia*
[d]*Micro System Technology (Centre of Excellence), Universiti Malaysia Perlis, Perlis, Malaysia*
[e]*Department of Computer Engineering, College of Computer Science and Engineering, University of Ha'il, Hail 55476, Saudi Arabia*
Corresponding author. Tel.: ++601112515077; e-mail: tijjani@unimap.edu.my

Received 25 April 2024, Revised 27 August 2024, Accepted 7 September 2024

ABSTRACT

This study introduces a novel methodology for mitigating mutual coupling in Terahertz (THz) multi-band Ultra-Massive Multiple-Input Multiple-Output (UM-MIMO) systems, specifically focusing on plasmonic nanoantenna arrays. The primary objective is to reduce the interference between Frequency Selective Surface (FSS) decoupling structures and adjacent nanoantenna array elements, which is critical for optimizing THz communication system performance. The research involves the design and characterization of new FSS structures and nanoantenna array geometries, employing advanced materials to enhance mutual coupling reduction. By precisely tuning the array geometry and refining the FSS decoupling structure, the study achieves a significant reduction in mutual coupling, with a frequency offset improvement of 4.7% relative to baseline frequencies. Furthermore, the integration of the optimized nanoantenna array with the FSS structure yields substantial reductions in return loss, with S_{11} and S_{22} values reaching approximately -7 dB and -8 dB, respectively. The proposed design also demonstrates a compact and stable configuration, achieving a uniform mutual coupling reduction of approximately -22 dB and FSS decoupling structure. This work provides a robust and efficient solution for enhancing the performance and reliability of multi-band THz UM-MIMO systems.

Keywords: *Nanoantenna array, Mutual coupling, Multi-band, Terahertz, 6th Generation communications, Ultra-Massive Multiple-Input Multiple-Output, Plasmonic graphene, Frequency selective surface.*

1. INTRODUCTION

Ultra-Massive MIMO (UM-MIMO) systems operating in the Terahertz (THz) frequency range represented a significant advancement in communication technology, offering the potential to achieve data rates and transmission speeds far exceeding those of traditional communication systems [1]. These systems were particularly distinguished by their capacity to support massive connectivity and high-speed data transfer, which were essential for emerging applications, such as 6G networks and beyond. As communication demands continued to grow, the focus increasingly shifted towards the development and integration of advanced nanoantenna arrays that could meet these high-performance requirements [2]. In the pursuit of realizing the full potential of UM-MIMO systems, researchers turned their attention to the use of linear array of plasmonic graphene-based nanoantennas, typically configured in a dipole arrangement [3]. These nanoantennas were selected for their exceptional properties, including wide bandwidth and the ability to achieve precise signal steering, making them ideal for deployment in highly dense communication environments [4].

The unique characteristics of graphene, such as its high electrical conductivity and flexibility at the nanoscale, further enhanced the performance of these antenna arrays, thereby driving their adoption in next-generation communication systems [5].

The literature on plasmonic graphene-based nanoantennas highlighted their numerous advantages, particularly in terms of bandwidth efficiency and their ability to mitigate interference through effective signal steering. Studies conducted by previous researchers had demonstrated that these antennas could significantly enhance communication performance in environments with high user density, where conventional antennas often struggled with interference and signal degradation. However, despite these benefits, the literature also underscored persistent challenges, particularly regarding mutual coupling between array elements [6]. This coupling, which occurred due to the proximity of the nanoantennas, had been identified as a critical factor that could degrade overall system performance [7]. While significant progress had been made in the design and application of graphene-based nanoantennas for UM-MIMO systems, there remained a notable gap in addressing the issue of mutual coupling. Existing studies had primarily focused on optimizing the individual performance of the nano-antennas, with less emphasis on understanding and mitigating the coupling effects that arose when these antennas were deployed in large arrays [8].

The impact of mutual coupling on system efficiency, particularly in terms of signal distortion, energy consumption, and the complexity of signal processing, had not been sufficiently explored. This gap in the literature indicated the need for further research to develop solutions that could minimize mutual coupling and enhance the overall performance of UM-MIMO systems [9, 10]. The objectives of the research were to investigate the impact of mutual coupling in UM-MIMO systems employing plasmonic graphene-based nano-antennas and to explore methods for mitigating these effects. Specifically, the study aimed to analyze the extent to which mutual coupling influenced system performance, including its effects on signal quality, energy efficiency, and processing complexity. Additionally, the research sought to identify and evaluate potential design modifications or signal processing techniques that could reduce mutual coupling, thereby improving the overall efficiency and reliability of UM-MIMO systems operating in the THz range.

2. METHODS

The study commenced with the design of a patch-dipole nanoantenna structure on a substrate devoid of a ground plane, aimed at creating dipole arms with a gap in the graphene patch material. The nanoantenna was reconfigurable with fixed dimensions and utilized a quartz SiO_2 substrate. The frequency tunability of the nanoantenna was exploited to optimize its performance. Subsequently, the design of the basic nanoantenna array element was calculated, including the determination of operational frequency and the length of the nanoantenna, with dimensions accordingly set. A simulation of the basic nanoantenna array element prototype was conducted to refine the dimensions and material properties. These modifications aimed to enhance performance, particularly to achieve a select operating frequency with a reflection coefficient (S_{11}) of less than -10 dB.

2.1. Single Nanoantenna Array Element Design

The section presented the basic nanoantenna arrays element design with model shown in Figure 1, where numerically calculated nanoantenna prototype was developed. The operation frequency (f) was set at 1.3 THz, angular frequency (ω) was calculated by ω = 2πf, graphene chemical potential was set at 0.3 eV, relaxation time (τ) was set at 1 ps, graphene temperature (T) set as 300 K, SiO_2 relative permittivity (Ɛ1) was set as 3.75, and air permittivity (Ɛ2) was set as 1. This followed by plasmon wavelength (λspp or Lspp) calculation using MATLAB, λspp was 79.049 µm. The nanoantenna dimensions are shown in Figure 1, where patch length (Pl) = patch width (Pw) and Pl were set as λspp/2-E*λspp/2, where G equals to E×λspp. Substrate height (h) was set as λspp/10 (Antenna Theory Analysis and Design Fourth Edition by Constantine A. Balanis, n.d.)[21], substrate length (L) and width (W) were set as a twice that of dipole length (experimentally). A 0.335-nm thickness graphene single layer was used for both patches in the dipole. A photoconductive source or a graphene-gated High-Electron-Mobility Transistor (HEMT) source is the approach used to feed the nanoantenna as demonstrated in the literature and design parameters are shown in Table 1 [4].

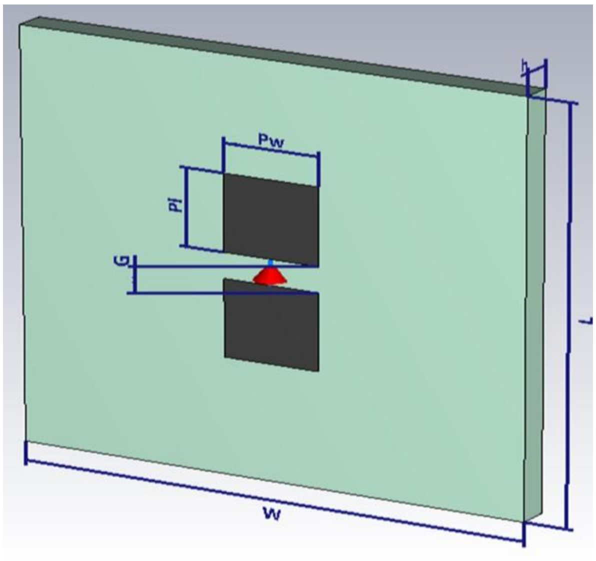

Figure 1. Single element design model

Table1. Single element nanoantenna design model specifications

Design Parameters	Expressions/Values	Description
f	1.3 THz	Operation Frequency
Graphene Chem. Potential	0.3 eV	Graphene Chem. Potential
τ	1 ps	Relax. Time
T	300 K	Graphene Temperature
thickness	0.335 nm	Patch Thickness
Ɛ1	3.75	SiO_2 Permittivity
Ɛ2	1	Air Permittivity
Lspp (λspp)	79.049 µm	SPP Wavelength
G	E × λspp	Dipole Patches
E	G/λspp	Gap ratio
Pl	(λspp/2-G)/2	Dipole Length
Pw	Pl	Dipole Width
L	2×(2×Pl+G)	Substrate Length
W	2×(2×Pw+G)	Width
h	λspp/10	Substrate Height

2. 2 Single Nanoantenna Array Element Design Optimization

In this section, the optimization of a single nanoantenna array element was performed, where S_{11} was tuned to the operational frequency of 1.3 THz by experimentally selecting various values for parameters and graphene relaxation time through simulations. The 'Parameter Sweep' and 'Optimizer' options were employed during the selection process. The optimization resulted in the setting of E=0.41E = 0.41E=0.41 and a graphene relaxation time of 0.95 ps. The optimized shape of the nanoantenna model is depicted in Figure 2, where the dimensions of the patches were significantly smaller compared to the substrate dimensions and the gap.

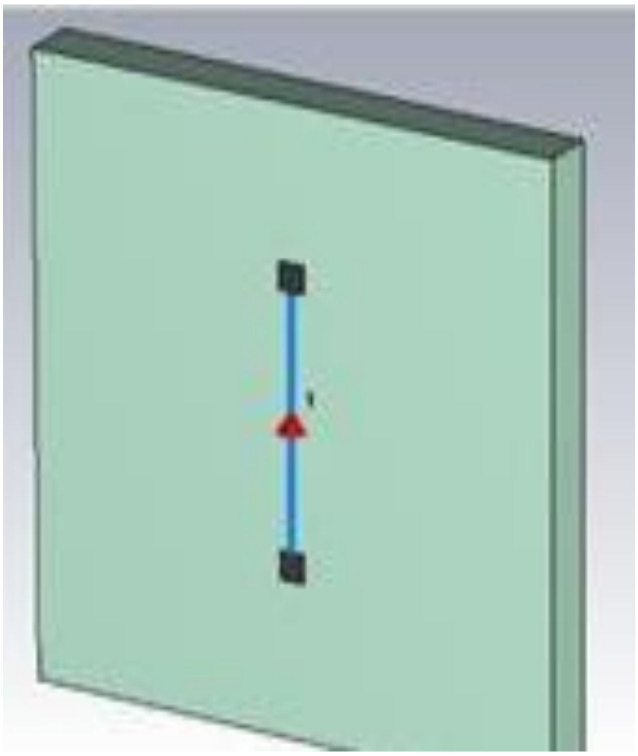

Figure 2. Nanoantenna model

Further, the patches dimensions (Pl, Pw) were fixed and then the gap was reduced by decreasing value of E until resonance of the nanoantenna was tuned to operation frequency, which leads to reducing the dimensions of the substrate, and finally getting a compact size for the nanoantenna. This allowed the nanoantenna model simulation Figure 2 by changing values of chemical potential from 0 eV to 1.2 eV in step of 0.1 for every based on the relaxation time of 0.55 ps, to explore reconfigurable frequency bands that the nanoantenna works on it efficiently (S_{11}< -10 dB). The setting mentioned for the nanoantenna frequency reconfigurability in the frequency range between 1.2532-2.1779 THz. Any two adjacent frequency bands within the range can be chosen, where a frequency of 1.3 THz was chosen by setting chemical potential of 0.3 eV for the first nanoantenna (Ant1), and a frequency of 1.4984 THz by setting chemical potential of 0.4 eV for the second nanoantenna (Ant2). Moreover, the specifications for the nanoantennas demonstrated varying performance metrics across different operational frequencies. Nanoantenna Ant1 operated at 1.3 THz with a graphene chemical potential of 0.3 eV, achieving a high S_{11} of -40 dB, indicating excellent impedance matching and minimal reflection losses. This nanoantenna exhibited a bandwidth of 0.10595 THz, reflecting its range of effective operation around the central frequency. The radiation efficiency was relatively low at 0.19%, suggesting that a significant portion of input power was not radiated effectively. The gain of Ant1 was not specified, but its directivity is 1.7 dBi, showing the ability to direct radiation in a specific direction. In contrast, Nanoantenna Ant2 operated at a higher frequency of 1.4984 THz with a graphene chemical potential of 0.4 eV. It had a lower S_{11} value of -16 dB, which was still indicative of good impedance matching but less effective than Ant1. Ant2 provided a broader bandwidth of 0.20175 THz, allowing for a more extensive range of operational frequencies. Its radiation efficiency was higher at 0.3%, which, while still modest, indicated improved performance over Ant1. The gain for Ant2 was not specified, but its directivity of 1.78 dBi reflected a slightly enhanced ability to focus radiation on a particular direction compared to Ant1. The specifications are shown in Table 2.

Table 2. The specification of the 2 element nanoant

Nanoantenna/ Specification	Operation Frequency	Graphene Chemical Potential	S_{11}	Bandwidth	Radiation Efficiency	Gain	Directivity
Ant1	1.3 THz	0.3 eV	-40 dB	0.10595 THz	0.19 %	-30 dBi	1.7 dBi
Ant2	1.4984 THz	0.4 eV	-16 dB	0.20175 THz	0.3 %	-25 dBi	1.78 dBi

2.3. 2-Element Nanoantenna Array Design

The design of the 2-element nanoantenna array followed the same methodology used for the single-element design. In this configuration, the array model was created with patch dipoles arranged in a linear interleaved pattern across the substrate, with a separation distance of 2 μm between each element. For the graphene definition, the first nanoantenna element was assigned a chemical potential of 0.3 eV, while the second element was set to 0.4 eV. This arrangement is depicted in Figure 3.

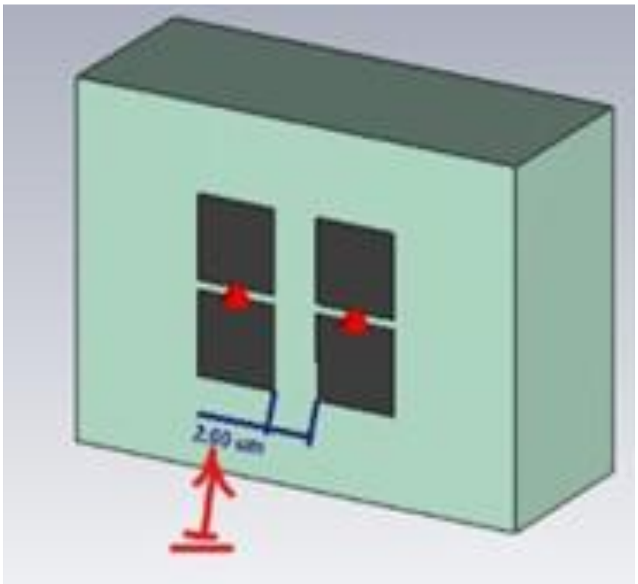

Figure 3. Nanoantenna array with the inter-element distance of 2 μm

2.4. Mutual Coupling Effect between the Nanoantenna Array Adjacent Elements

The mutual coupling effect between the two nanoantenna array elements was assessed by analyzing S_{11}S{11}S_{11}, S_{21}S_{21}S_{21}, S_{22}S{22}S_{22}, and the Envelope Correlation Coefficient (ECC), as illustrated in Figure 3. To determine the ECC, 'postprocessing' was selected, followed by choosing 'result templates' under 'Tools'. This opened the 'template based post-processing' window, where both 'farfield and antenna properties' and 'Diversity Gain and Correlation (from *S*-parameters)' were configured. In the 'Diversity Gain (from *S*-parameters)' window, the 'correlation Coefficient' option was selected and confirmed by clicking 'OK'. The 'Evaluate' button was then clicked, resulting in 'Env_Corr_Coeff from S' appearing in the 'Navigation Tree' under 'Tables'. Clicking on this entry displayed the ECC curve, as shown in Figure 3.

$$2L + G \cong {}^{\lambda_0}/_{2} \qquad (1)$$

$$L = \frac{\lambda_{SPP}}{2} \qquad (2)$$

2.5 Reconfigurable-Frequency Selective Surface (FSS) Structure Unit Cell Design for Decoupling

The Frequency Selective Surface (FSS) structure unit cell was mathematically designed, simulated, and optimized to achieve S_{21} < -15dB within the target frequency range while maintaining a compact size suitable for integration with the previously designed 2-element nanoantenna array model. The unit cell of the FSS structure comprises four patch dipoles separated by three dielectric layers. Dipole 1 and dipole 4 patches are aligned on a quartz (SiO_2) layer, positioned between two layers of air and quartz. In contrast, dipole 2 and dipole 3 patches were situated between layers of quartz and polysilicon and were oriented perpendicular to dipole 1 and dipole 4. Patches material consisted of single layer graphene, where graphene chemical potentials were set to 0.3 eV for both dipole 1 and dipole 2 while for both dipole 3 and dipole 4 were set to 0.4 eV. Graphene relaxation time set to 0.8 ps, and graphene temperature was set on 300 K. Based on Equation 1, length of dipole 1 patch (Plo) was set from the equation ((Lsppo/2-Go)/2), where dipole 1 gap (Go) was set as (Go= O×Lsppo), dipole 1 width (Pwo) was set as (Pwo = Plo). Plasmon wavelength of dipole 2 (Lsppi) was calculated similarly to dipole 1 calculation using plasmon wavelength with difference from surrounding dielectric layers, SiO_2 relative permittivity (Ɛ1) was set to 3.75 and polysilicon relative permittivity (Ɛ2) was set to 11.9. Then dipole 1 patch length (Pli) was set based the equation 2 (Pli=(Lsppi/2Gi)/2), where dipole gap was set on (Gi=k×Lsppi), and patch width (Pwi) was set as (Pwi = Pli). Figure 4 shows dimensions of previous four dipoles and the layers and displayed all dimensions shown that were set as dipoles 1 and 4 dimensions were same, and dipoles 2 and 3 as shown in Figure 4.

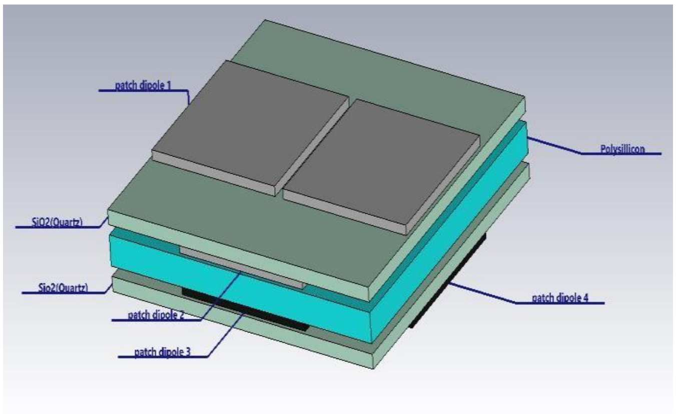

Figure 4. FSS structure unit cell configuration for the antenna

The design parameters for the FSS structure were integral to optimizing the nanoantenna system's performance. The dimensions of the polysilicon layer were determined by its length and width, which were both calculated to be twice the length of the dipole 1 patch plus the gap between dipoles. The thickness of the polysilicon layer was set to one-tenth of the plasmon wavelength of dipole 1, as specified in Table 2. Similarly, the dimensions of the SiO_2 layers were also based on the length and width formulas used for the polysilicon layer. The thickness of these quartz layers was set to one-tenth of the plasmon wavelength of dipole 2. The plasmon wavelengths for dipole 1 and dipole 2 were pre-defined values that played a crucial role in determining the optical properties and effectiveness of the FSS structure. For the dipole patches, their lengths and widths were determined by adjusting them based on the plasmon wavelengths and the gaps between dipoles. The gaps were calculated based on specific ratios, which were experimentally determined. These parameters ensured that the dipole patches and their gaps were optimized to enhance frequency selectivity and reduce interference between the dipoles.

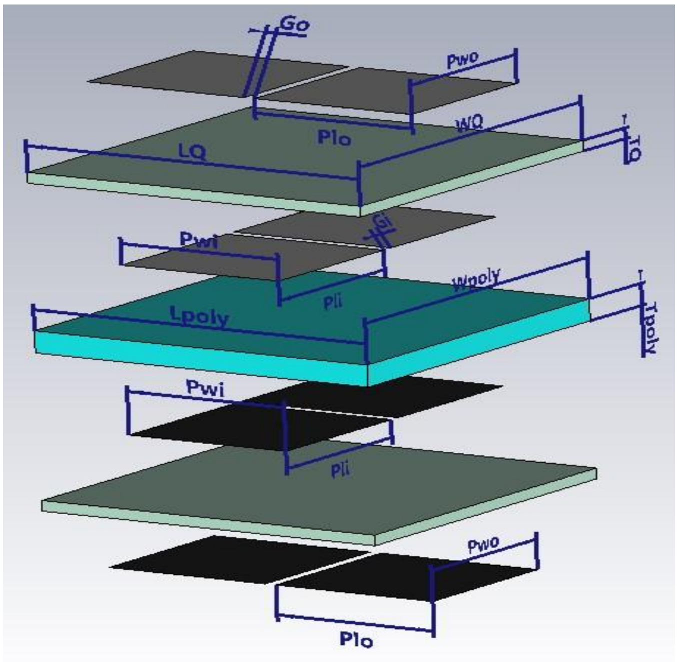

Figure 5. FSS structure unit cell dimensions

Table 3. FSS dimensions

Design parameters	Expression	Description
Lpoly	2×Plo+Go	length
Wpoly	2×Plo+Go	width
Tpoly	Lsppo/10	thickness
LQ	2×Plo+Go	SiO_2 length
WQ	2×Plo+Go	SiO_2 width
TQ	Lsppi/10	SiO_2 thickness
Lsppo	79.049 μm	Plasmon dipole 1
Lsppi	23.993 μm	Plasmon dipole 2
Plo	(Lsppo/2-	dipole 1 patch
Pwo	Plo	Width of dipole 1
Go	E×Lsppo	dipole 1 gap
Pli	(Lsppi/2-Gi)/2	dipole 2 patch
Pwi	Pli	Width dipole 2
Gi	O×Lsppi	dipole 1 gap
E, O	By simulation	Gap Ratio

2.6. FSS structure unit cell simulation

After obtaining the FSS structure unit cell dimensions from Table 3, the simulation of the prototype was initiated using CST software. The FSS structure model was set up by selecting "Periodic Structures" instead of "Antennas." The simulation utilized the "FSS, Metamaterial - Unit Cell" option, based on the "Phase Reflection Diagram" in the frequency domain. The units were configured as micrometers (μm), terahertz (THz), picoseconds (ps), and kelvin (K), with the frequency range set for the stop band between 0.1 THz and 3.3 THz. This process adhered to the flowchart outlined in Figure 6.

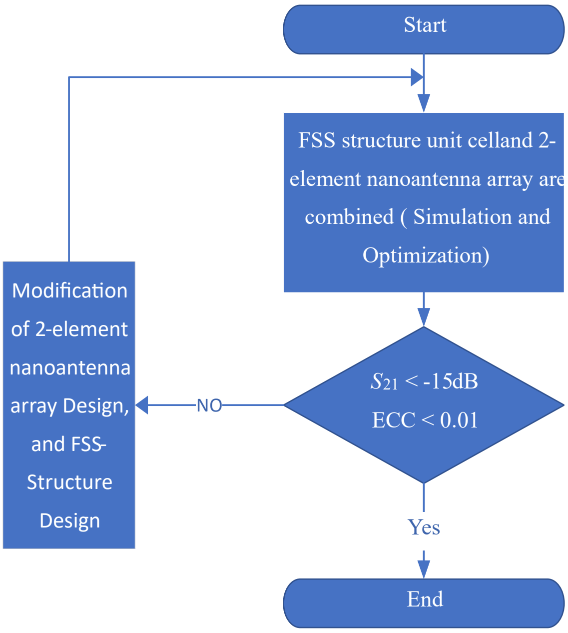

Figure 6. Combination of FSS structure and 2-element nanoantenna array flowchart

3. RESULTS AND DISCUSSION

3.1 Single Element Design of Nanoantenna Array

Table 4 shows results of Single Element Design of Nanoantenna Array with plasmon wavelength for the dipole antenna set at 3.7 μm. This parameter is crucial as it defined the wavelength at which surface plasmon resonances occurred on the dipole patches. A precise plasmon wavelength ensured optimal resonance conditions and affects the antenna's ability to interact with electromagnetic waves effectively. The chosen value was a balance between achieving strong plasmonic effects and maintaining practical dimensions for integration into the antenna design.

Table 4. Single Element Design of Nanoantenna Array

Name	Expression	Value	Description
Lspp		3.7 μm	wavelength
E		0.0045	Gap ratio
G	E×Lspp	0.3557205 μm	dipole patches gap.

Pl		3.16196 µm	Patch length
Pw	Pl×0.875	2.766715 µm	Patch width
L		13.359281 µm	Substrate length
W		13.359281 µm	Substrate width
h	Lspp/25	3.16196 µm	Substrate height
thickness		0.335 nm	
temperature		300 k	
Potential		0.3 eV	
relax Time		0.8 ps	

The gap ratio between the dipole patches was defined by the parameter E, which was set at 0.0045. This ratio represents the proportion of the gap distance relative to the plasmon wavelength. A smaller ratio indicated a tighter gap, which could influence the coupling and resonance characteristics of the dipole patches. This parameter was critical for fine-tuning the antenna's performance and ensuring that the gap between patches aligned with the desired resonance conditions. Gap Between Dipole Patches (G): Calculated as the product of the gap ratio (E) and the plasmon wavelength (Lspp), the gap between the dipole patches is 0.3557205 µm. This dimension was significant for determining how closely the dipole patches were positioned relative to each other, impacting the mutual coupling and overall antenna efficiency. A well-chosen gap size helped in minimizing interference and optimizing the antenna's performance. Dipole Patch Dimensions (Pl and Pw): The length (Pl) of the dipole patch was set to 3.16196 µm, and the width (Pw) was calculated as 87.5% of the length, resulting in 2.766715 µm. These dimensions were essential for achieving the desired electromagnetic characteristics, such as resonant frequency and radiation patterns. Accurate patch dimensions ensured that the dipole patches were appropriately sized to resonate at the targeted plasmon wavelength.

Substrate Dimensions and Material Properties: The substrate length (L) and width (W) were both 13.359281 µm, while the height (h) is 3.16196 µm, calculated as one twenty-fifth of the plasmon wavelength. These dimensions defined the size and thickness of the substrate supporting the dipole patches. The choice of a 0.335 nm thick graphene layer with a temperature of 300 K, a chemical potential of 0.3 eV, and a relaxation time of 0.8 ps further influenced the performance of the nanoantenna. These properties were critical for determining the electronic and thermal behaviour of the graphene layer, affecting the overall efficiency and resonance of the antenna design.

Figures 7(a) and (b) displayed the S_{11} parameter for graphene with chemical potentials set to 0.3 eV and 0.4 eV. Figure 7(b) illustrates the target frequency range of operation for the frequency-reconfigurable nanoantenna array, which spanned from 1.264 THz to 1.964 THz with S_{11} values below -10 dB. The first basic element of the nanoantenna array (Ant1) operated at a resonant frequency of 1.3 THz, while the second basic element (Ant2) operated at 1.4952 THz, both of which fall within the target frequency range. The basic elements also demonstrated efficient operation within this range, with potential frequencies extended to configurations, such as 0.4 eV to 0.5 eV or 0.5 eV to 0.6 eV. Additionally, the achieved bandwidth for the target frequency range was approximately 0.7 THz.

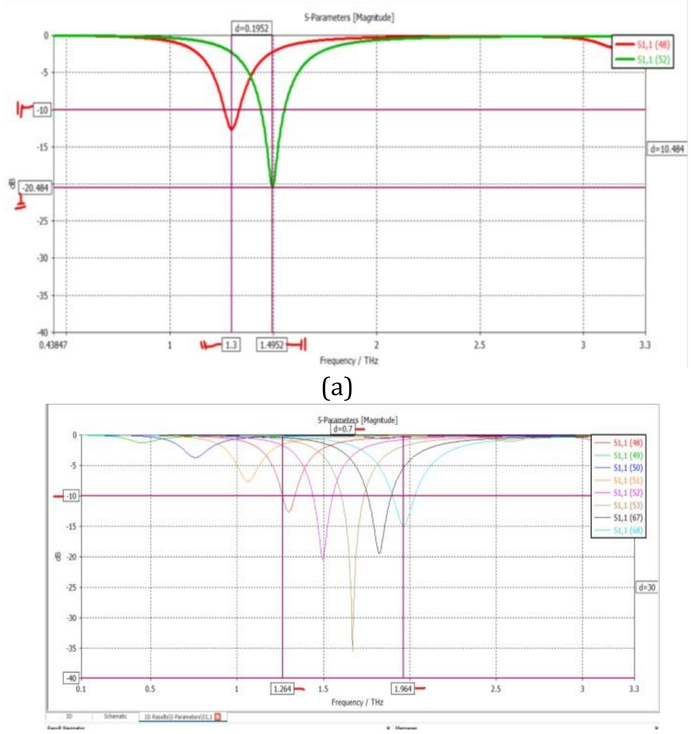

(a)

(b)

Figure 7. (a) S_{11} with two chemical potentials 0.3 eV, 0.4 eV (b) Target frequency range

3.2. 2-Element Nanoantenna Array Design and Mutual Coupling between Two Nanoantenna Array Elements

In Figure 8(a), the results indicate that at 2 µm, the peak value of the S_{21} curve was approximately -13.96 dB. This value was higher than the acceptable threshold of -15 dB, which signified insufficient efficiency for the nanoantenna array system, as evidenced by the S_{11} and S_{22} curves. Figure 8(b) presents the Envelope Correlation Coefficient (ECC) curve, demonstrated an imbalance among the S_{11}, S_{22}, and S_{21} values. For optimal performance, the ECC should be below 0.01, highlighting that the current design did not meet this requirement.

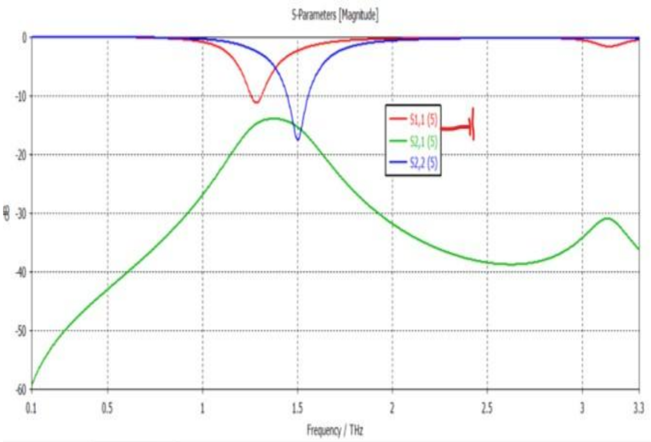

(a)

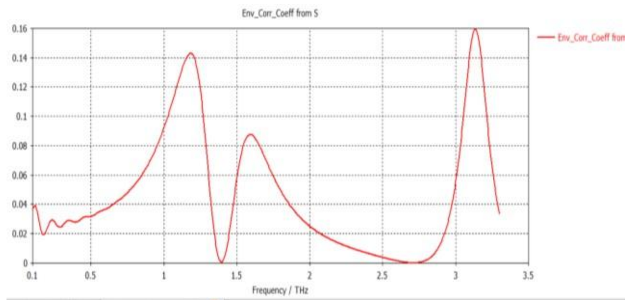

(b)

Figure 8. (a) S_{11}, S_{21}, and S_{22} parameters (b) ECC curve

The reconfigurable-frequency Frequency Selective Surface (FSS) structure was developed using single-layer graphene for all dipole patches, as described in the literature. Each dipole patch had uniform dimensions, and the gaps between all dipoles were identical. The width of each patch was twice the length of the patch. The dipoles were positioned centrally within the dielectric layers. The relative permittivity of quartz (SiO_2) was set to 3.75, while that of polysilicon was 11.9. The graphene patches were assigned different chemical potentials: black patches were set to 0.4 eV, and gray patches to 0.3 eV. The FSS structure was integrated with a 2-element nanoantenna array, achieving a compact design. The FSS structure was centred vertically between the two nanoantenna elements (Ant1 and Ant2), with a separation of 2 μm. Additionally, the colour arrangement of the dipole patches in the FSS structure was consistent with that of the nanoantenna array elements: black graphene patches (0.4 eV) were grouped together, and gray graphene patches (0.3 eV) were also grouped together.

The proposed design for the nanoantenna array features a compact configuration, optimizing space and integration within a subarray for smaller UM-MIMO systems. The dimensions of the basic element nanoantenna were meticulously designed, with an antenna height of approximately 3.5 μm, a width of around 13.4 μm, and a dipole patch width of about 3.2 μm. The distance between the two array elements was set to approximately 2 μm, aligning with the subarray's linear geometry, which contributes to reducing the overall width. The FSS decoupling structure, with a height of about 6.7 μm, also played a crucial role in minimizing the array height. The use of rectangular patch dipole shapes in both the basic nanoantenna array elements and the FSS unit cell simplified the design, ensuring ease of integration and uniformity without altering the array structure [19].

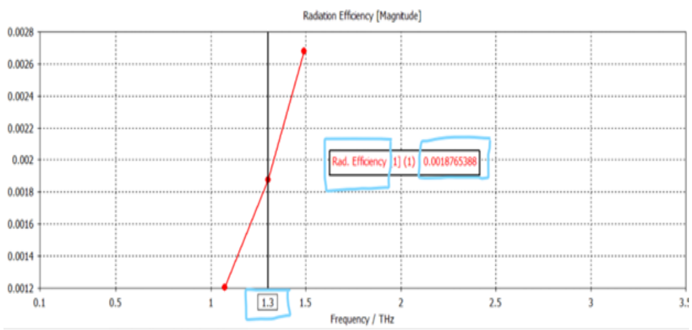

(a)

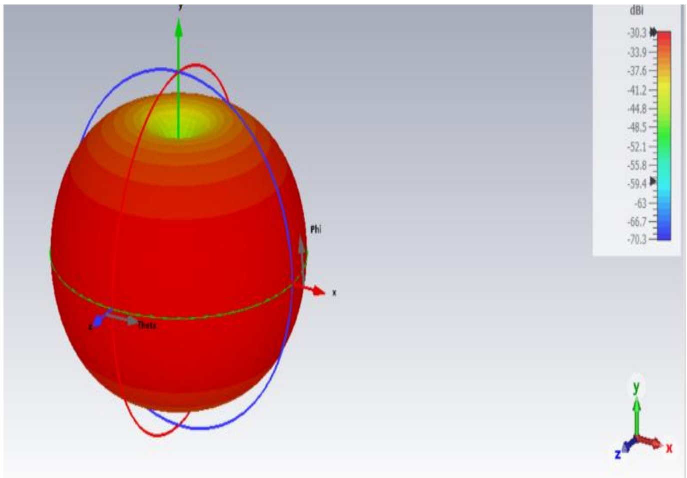

(b)

Figure 9. (a) Efficiency (b) Gain / Directivity

Despite the compact design, there is a trade-off in terms of performance. The basic nanoantenna elements exhibited reduced radiation efficiency and gain as in Figure 9 (a and b). Specifically, Ant1 and Ant2 achieved efficiencies of 0.12% and 0.21% at operating frequencies of 1.3 THz and 1.4952 THz, respectively, with gains of -30.3 dBi and -25 dBi. However, higher efficiency and gain could be achieved at other tuned frequencies within the target range of 1.264 to 1.964 THz. The relaxation time of single-layer graphene, modelled in the CST software, was approximately 0.8 ps for both the basic nanoantenna elements and the FSS structure. This relaxation time impacts mutual coupling, initially causing significant coupling with an S_{21} value of about -13.96 dB but reducing mutual coupling by more than 8 dB after integrating the FSS structure [20].

Graphene characterization further enhanced performance by mitigating mutual coupling between the FSS structure and the nanoantenna elements. The frequency offset for Ant1 and Ant2 was approximately 4.7% relative to their original frequencies. The gain variations for Ant1 and Ant2 are minimal, with maximum deviations of -2 dBi and -4.2 dBi, respectively, and a change of less than 0.1 dB for Ant1.

Notably, the directivity of Ant1 and Ant2 improved by 0.24 dBi and 0.14 dBi, respectively, compared to their original values. This demonstrates the effectiveness of the design in enhancing performance while maintaining compactness and integration efficiency. The incorporation of advanced graphene characterization techniques has significantly improved the balance between mitigating mutual coupling among the two array elements and between the array elements and the FSS structure. This balanced approach leads to a substantial reduction in the return loss for both array elements, Ant1 and Ant2. Specifically, the values of S_{11} and S_{22} were reduced to approximately -7 dB and -8 dB, respectively, across both operating frequencies. This enhancement in return loss indicates a more efficient performance of the nanoantenna array, with less signal reflection and improved signal integrity. Moreover, by fine-tuning the dimensions of the patch dipoles in the FSS structure and adjusting the graphene relaxation time, the Envelope Correlation Coefficient (ECC) had been successfully reduced to less than 0.01. This low ECC value signified that the mutual coupling between the array elements was minimized, ensuring that the performance of each element was less affected by the presence of adjacent elements and the FSS structure. These adjustments contributed to achieving high performance and stability in the nanoantenna array system, demonstrating the effectiveness of the new graphene characterization in optimizing the system's overall functionality. Table 5 enlists the summary of the performance results of the proposed design.

Table 5. Results summary

Parameter	Current Study
Directivity of Ant1	Improved by 0.24 dBi
Directivity of Ant2	Improved by 0.14 dBi
Mutual Coupling Reduction	Mitigated by more than 8 dB
Frequency Offset	Approximately 4.7% relative to original frequencies
S_{21} Value (before FSS)	Approximately -13.96 dB
Graphene Relaxation Time	0.8 ps for both elements and FSS structure
Bandwidth of Frequency Range	Achieved approximately 0.7 THz

In the current study, the directivity of Ant1 and Ant2 improved by 0.24 dBi and 0.14 dBi, respectively. This enhancement in directivity indicated that the overall radiation pattern of the antennas became more focused, which was a significant improvement over the performance metrics reported in previous studies. Improved directivity typically enhanced the antenna's ability to transmit or receive signals more efficiently in a specific direction, leading to better performance in practical applications. The mutual coupling between the array elements was mitigated by more than 8 dB in the current study. This was a noteworthy improvement, as mutual coupling reduction was crucial for minimizing interference between antenna elements, leading to better signal integrity and system performance. The significant reduction in mutual coupling suggested that the use of the FSS structure effectively isolated the antenna elements, enhancing the overall performance of the nanoantenna array. The frequency offset for each antenna element was approximately 4.7% relative to the original frequencies. This offset reflected the deviation of the antenna resonant frequencies from their intended targets, which could impact the precision of frequency-specific applications. The 4.7% offset indicated a moderate adjustment requirement, which was generally manageable but highlights the need for further fine-tuning to achieve optimal frequency performance. Before the implementation of the FSS structure, the S_{21} value was approximately -13.96 dB. This value indicated the level of signal transmission between the two antenna elements, with a higher (less negative) S_{21} value reflecting better signal coupling. The relatively low value of -13.96 dB suggested that mutual coupling was significant prior to the application of the FSS structure, supporting the need for its introduction to improve coupling characteristics. The relaxation time of graphene was set to 0.8 ps for both the antenna elements and the FSS structure, played a critical role in determining the material's electrical properties and overall performance.

This relaxation time was consistent with typical values used in similar studies, ensuring that the graphene's response time was adequate for effective operation within the nanoantenna system. The current study achieved a bandwidth of approximately 0.7 THz for the frequency range, which was a substantial bandwidth relative to previous research. This broad bandwidth indicated that the nanoantenna array could operate effectively across a wide range of frequencies, enhancing its versatility and performance in different applications. Overall, the current study demonstrated significant improvements in several key performance metrics of the nanoantenna array compared to prior research. The enhancements in directivity and mutual coupling reduction, along with the effective bandwidth and controlled frequency offset, reflect the successful integration of the FSS structure and the optimization of graphene properties. These advancements contribute to the development of more efficient and high-performing nanoantenna systems.

Table 6. Comparison of Decoupling Structures, Operating Frequencies, Decoupling Improvements, and Reconfigurability Across Various Studies.

Ref.	Doubling structure	Operating Frequency (THz)	Decoupling (dB)	Reconfigurability
Current Study	Graphene	1.3	-22	Yes
[11]	Graphene	6	30.42	Yes
[12}	Graphene Metal	1.1	-15	NO
[13]	Metal	3 GHz	-23	NO
[14]	Graphene	4.5	6	YES
[15]	Metal	25	−20	NO

Ref.	Doubling structure	Operating Frequency (THz)	Decoupling (dB)	Reconfigurability
[16]	Metal	5.6	7.2	NO
[17]	Graphene	1.1	-15	NO
[18]	Graphene	10	-	NO

This table compares various studies that focus on decoupling structures for operating frequencies, decoupling improvements, and reconfigurability in the THz range, emphasizing different materials like graphene and metal. The current study stands out by employing graphene as the material for the decoupling structure, operating at a frequency of 1.3 THz, achieving a decoupling improvement of -22 dB, and incorporating reconfigurability. When compared to other studies in the table, this study demonstrates a balanced performance in terms of decoupling improvement and reconfigurability, making it a unique contribution to the field. Firstly, examining the material choices reveals that graphene is the predominant material for decoupling structures in these studies, with a few using metal.

The current study's use of graphene at 1.3 THz is significant, as it operates at a frequency lower than most graphene-based studies, such as [11] and [14], which operate at 6 THz and 4.5 THz, respectively. Although [11] achieves a higher decoupling improvement of 30.42 dB, the current study's reconfigurability adds a distinct advantage, highlighting its potential in adaptable applications. This contrasts with [12], which also uses a combination of graphene and metal but lacks reconfigurability and shows a lower decoupling improvement at 1.1 THz. Secondly, the studies utilizing metal for the decoupling structure generally show mixed results regarding decoupling improvement and reconfigurability. For instance, [13] achieves a decoupling improvement of -23 dB at a much lower frequency of 3 GHz, but it does not offer reconfigurability. Similarly, [15] and [16] operate at higher frequencies of 25 THz and 5.6 THz, with decoupling improvements of -20 dB and 7.2 dB, respectively, but again lack reconfigurability. This comparison underscores the novelty of the current study, which not only achieves significant decoupling improvement but also incorporates reconfigurability, making it more versatile in real-world applications. Lastly, the reconfigurability aspect is a crucial factor that differentiates the current study from others.

Reconfigurability allows for dynamic adaptation to changing conditions, making the technology more suitable for advanced communication systems and other applications requiring flexibility. Among the studies listed, only a few, such as [11] and [14], incorporate reconfigurability, but their decoupling improvements and operating frequencies either exceed or do not match the balance achieved in the current study. This balance of decent decoupling improvement and reconfigurability at a lower THz range solidifies the study's novelty in the ongoing research landscape. In conclusion, the current study presents a novel contribution by effectively balancing decoupling improvement and reconfigurability at a lower operating frequency of 1.3 THz using graphene. While other studies show higher decoupling improvements or operate at different frequencies, the inclusion of reconfigurability at this frequency range sets the current study apart. This unique combination of features makes it a valuable addition to the field, especially in applications where adaptability and effective decoupling are critical. Especially, in an application such as autonomous vehicles [22, 23].

4. CONCLUSION

This study introduces a novel design approach for UM-MIMO systems, with a primary focus on reducing mutual coupling between antenna array elements. The research emphasized the importance of optimizing the geometry of a basic nanoantenna array element to achieve these objectives. The proposed design incorporated a newly developed Frequency Selective Surface (FSS) decoupling structure, which played a crucial role in mitigating the mutual coupling between the antenna array elements. The nanoantenna array element was designed to be compact, which, while reducing the overall structure size, also impacted radiation efficiency and gain. Specifically, the efficiency of the antenna reached 0.12%, and the gain values were recorded at -30.3 dBi for Ant1 and -25 dBi for Ant2 at the operating frequencies of 1.3 THz and 1.4952 THz, respectively.

However, higher efficiency and gain were observed at other tuned frequencies within the target range, demonstrating the versatility of the design. One of the key achievements of this study was the effective reduction of mutual coupling not only between the antenna array elements but also between the FSS decoupling structure and the array elements. This was proven by a frequency offset of approximately 4.7% relative to the original frequencies. Additionally, the gain values for Ant1 and Ant2 improved by -2 dBi and -4.2 dBi, respectively, compared to their original directivity values. Furthermore, the proposed design led to a significant reduction in the return loss for both array elements, with S_{11} and S_{22} values reaching approximately -7 dB and -8 dB, respectively. This innovative approach ensured a smaller and more stable structure while maintaining effective performance across the desired frequency range. The integration of the FSS decoupling structure onto the nanoantenna array substrate without altering the array's geometry contributed to the uniformity and stability of the design, making it a promising solution for advanced UM-MIMO systems. The balance between size reduction and performance enhancement highlighted the potential of this design for future high-frequency communication systems, where compactness and efficiency were dominant, respectively.

REFERENCES

[1] Y. Zhu, Y. Chen, and S. Yang, "Cross-Band Mutual Coupling Reduction in Dual-Band Base Station Antennas with a Novel Grid Frequency Selective Surface," *IEEE Trans. Antennas Propag.*, vol. 69, no. 12, pp. 8991–8996, Dec. 2021.

[2] S. Dash, C. Liaskos, I. F. Akyildiz, and A. Pitsillides, "Nanoantennas design for THz communication: Material selection and performance enhancement," *Proc. 7th ACM Int. Conf. Nanoscale Comput. Commun.*, NanoCom 2020, Sep. 2020.

[3] X. Zou, G. Wang, Y. Wang, and B. Zong, "Metasurface-based coupling suppression for sideband multiple-input-multiple-output antenna arrays," *Opt. Express*, vol. 29, no. 25, p. 41643, Dec. 2021.

[4] Y. Zhu, Y. Chen, and S. Yang, "Decoupling and low-profile design of dual-band dual-polarized base station antennas using frequency-selective surface," *IEEE Trans. Antennas Propag.*, vol. 67, no. 8, pp. 5272–5281, Aug. 2019.

[5] Z. Zhang, K. Wei, J. Xie, J. Li, and L. Wang, "The MIMO antenna array with mutual coupling reduction and cross-polarization suppression by defected ground structures," *Radioengineering*, vol. 27, no. 4, pp. 969–975, Dec. 2018, doi: 10.13164/re.2018.0969.

[6] S. Dey, D. Chatterjee, E. J. Garboczi, and A. M. Hassan, "Plasmonic Nanoantenna Optimization Using Characteristic Mode Analysis," *IEEE Trans. Antennas Propag.*, vol. 68, no. 1, pp. 43–53, Jan. 2020.

[7] H. Alwareth et al., "A Wideband High-Gain Microstrip Array Antenna Integrated with Frequency-Selective Surface for Sub-6 GHz 5G Applications," *Micromachines*, vol. 13, no. 8, Aug. 2022.

[8] A. K. Baranwal and N. P. Pathak, "Enhanced Gain triangular patch nanoantenna using Hybrid plasmonic waveguide on SOI technology," *Proc. 2019 IEEE Indian Conf. Antennas Propag.*, InCAP 2019, Dec. 2019, pp. 15–17.

[9] W. Amara, D. Oueslati, N. Eltresy, A. Alghamdi, K. Sedraoui, T. Aguili, H. Rmili, and R. Mittra, "Parametric study of modified dipole nano-antennas printed on thick substrates for infrared energy harvesting," Int. J. Numer. Model. Electron. Netw. Devices Fields, vol. 33, no. 2, 2020.

[10] A. Askarian, J. Yao, Z. Lu, and K. Wu, "Surface-Wave Control Technique for Mutual Coupling Mitigation in Array Antenna," *IEEE Microw. Wireless Compon. Lett.*, vol. 32, no. 6, pp. 623–626, Jun. 2022.

[11] N. K. Maurya, S. Kumari, P. Pareek, and L. Singh, "Graphene-based frequency agile isolation enhancement mechanism for MIMO antenna in terahertz regime," *Nano Commun. Netw.*, vol. 35, 2023, Art. no. 100436. doi: 10.1016/j.nancom.2023.100436.

[12] B. Zhang, J. Jornet, I. Akyildiz, and Z. Wu, "Mutual Coupling Reduction for Ultra-Dense Multi-Band Plasmonic Nano-Antenna Arrays Using Graphene-Based Frequency Selective Surface," *IEEE Access*, vol. PP, pp. 1–1, 2019. doi: 10.1109/ACCESS.2019.2903493.

[13] G. A. Fadehan, Y. O. Olasoji, and K. B. Adedeji, "Mutual Coupling Effect and Reduction Method with Modified Electromagnetic Band Gap in UWB MIMO Antenna," *Appl. Sci.*, vol. 12, no. 23, p. 12358, 2022. doi: 10.3390/app122312358.

[14] A. A. Ibrahim and S. M. Gaber, "Frequency reconfigurable antipodal Vivaldi 2-port antenna based on graphene for terahertz communications," *Opt. Quant. Electron.*, vol. 55, p. 786, 2023. doi: 10.1007/s11082-023-05036-9.

[15] T. Islam, F. Alsaleem, F. Alsunaydih, and K. Alhassoon, "Mutual Coupling Reduction in Compact MIMO Antenna Operating on 28 GHz by Using Novel Decoupling Structure," *Micromachines*, vol. 14, no. 11, p. 2065, Nov. 2023. doi: 10.3390/mi14112065.

[16] X. Zhu, X. Yang, Q. Song, et al., "Compact UWB-MIMO antenna with metamaterial FSS decoupling structure," *J. Wireless Com. Netw.*, vol. 2017, p. 115, 2017. doi: 10.1186/s13638-017-0894-3.

[17] B. Zhang, J. Jornet, I. Akyildiz, and Z. Wu, "Graphene-based frequency selective surface decoupling structure for ultra-dense multi-band plasmonic nano-antenna arrays," in *Proc. 5th ACM Int. Conf. Nanoscale Comput. Commun.*, NANOCOM, 2018, pp. 1–6. doi: 10.1145/3233188.3233211.

[18] L. Zakrajsek, E. Einarsson, N. Thawdar, M. Medley, and J. Jornet, "Design of Graphene-based Plasmonic Nano-antenna Arrays in the Presence of Mutual Coupling," in *Proc. Eur. Conf. Antennas Propag.*, EuCAP, 2017. doi: 10.23919/EuCAP.2017.7928818.

[19] K. Muthukrishnan, M. M. Kamruzzaman, S. Lavadiya, and V. Sorathiya, "Superlative split ring resonator shaped ultrawideband and high gain 1×2 MIMO antenna for Terahertz communication," *Nano Commun. Netw.*, vol. 36, 2023, Art. no. 100437. doi: 10.1016/j.nancom.2023.100437.

[20] T. Islam, F. Alsaleem, F. Alsunaydih, and K. Alhassoon, "Mutual Coupling Reduction in Compact MIMO Antenna Operating on 28 GHz by Using Novel Decoupling Structure," *Micromachines*. doi: 10.3390/mi14112065.

[21] C. A. Balanis, *Antenna Theory: Analysis and Design*, 4th ed., Hoboken, NJ, USA: Wiley, 2026.

[22] A. K. Y. Dafhalla et al., "Computer-Aided Efficient Routing and Reliable Protocol Optimization for Autonomous Vehicle Communication Networks," *Computers*, vol. 14, no. 1, p. 13, 2025.

[23] A. K. Y. Dafhalla et al., "High-Performance Data Throughput Analysis in Wireless Ad Hoc Networks for Smart Vehicle Communication Networks," Computers, vol. 14, no. 2, p. 56, 2025.